Supplementary Information for

[MoS] Insertion Chains Induced Small-Polaron Collapse in MoS_2 2D Layers: A Novel Mo_2S_3 Anode for Ultrafast Sodium Storage

Zhuoran Lv,[1,3,#] Chendong Zhao,[1,3,#] Miao Xie,[1,3,#] Mingzhi Cai,[4] Baixin Peng,[1,3] Dayong Ren,[1] Yuqiang Fang,[1] Wujie Dong,[1] Wei Zhao,[1] Tianquan Lin,[5] Ximeng Lv,[2,*] Gengfeng Zheng,[2] and Fuqiang Huang[1,3,4,*]

[1] State Key Laboratory of High Performance Ceramics and Superfine Microstructure, Shanghai Institute of Ceramics, Chinese Academy of Sciences, Shanghai 200050, China.

[2] Laboratory of Advanced Materials, Department of Chemistry and Shanghai Key Laboratory of Molecular Catalysis and Innovative Materials, Fudan University, Shanghai 200438, China.

[3] Center of Materials Science and Optoelectronics Engineering, University of Chinese Academy of Sciences, Beijing 100049, China.

[4] State Key Laboratory of Rare Earth Materials Chemistry and Applications, College of Chemistry and Molecular Engineering, Peking University, Beijing 100871, China.

[5] School of Materials Science and Engineering, Shanghai Jiao Tong University, Shanghai 200240, China.

# These authors contributed equally to this work.

* Corresponding authors: ximeng_lv@fudan.edu.cn, huangfq@mail.sic.ac.cn

Experimental Section

Chemicals. All chemicals in this work were used directly without further purification: Nano Mo powder (99.99%, Aladdin); S powder (99.95%, Aladdin); NaCl (99.5%, Sigma-Aldrich); Red phosphorus (99%, Aladdin). Deionized water used was in-house generated (resistivity: 0.860 MΩ cm at 25 ℃, which is measured by Rex DDSJ-308F Conductivity Meter).

Synthesis of Mo_2S_3. Mo_2S_3 was synthesized via a molten salt-assisting solid-state reaction. Mo powder and S powder were ground uniformly in the molar ratio of 2:3 with NaCl (5 times the mass) and 2.5 wt.% red phosphorus. The mixed powders were sealed in an evacuated quartz tube, which was transferred into a muffle furnace and heated at a rate of 2 ℃ min^{-1} to 900 ℃ and kept for 24 h. After naturally cooling to room temperature, the product was collected and soaked in deionized water to remove NaCl and dried at 80 ℃ for 12 h to obtain the Mo_2S_3 sample.

Synthesis of MoS_2. MoS_2 was synthesized via a solid-state reaction. Mo powder and S powder were ground uniformly in the molar ratio of 1:2. The mixed powders were sealed in an evacuated quartz tube, which was transferred into a muffle furnace and heated at a rate of 2 ℃ min^{-1} to 850 ℃ and kept for 24 h to obtain the MoS_2 sample.

Material Characterization. The X-ray diffraction (XRD) characterization was carried out on a Bruker D8 Advance diffractometer operating with a Cu Kα radiation (λ=1.5406 Å). Raman spectroscopy was conducted on a Jobin-Yvon LabRAM HR-800 spectrometer with a laser excitation wavelength of 532 nm. The in situ XRD and Raman

measurements were conducted using the operando battery cases at a constant current density of 100 mA g^{-1}. Scanning electron microscopy (SEM) images were obtained by a JEOL (JSM6510) scanning electron microscope. Transmission electron microscopy (TEM) observations were carried out on a JEOL (JEM-2100F) transmission electron microscope. X-ray photoelectron spectroscopy (XPS) measurements were conducted on a Thermo Scientific Escalab 250 X-ray photoelectron spectrometer. Temperature-dependent resistivity measurements were performed using a Physical Properties Measurement System (PPMS, Quantum Design). For the electric property test, the sample powder was pressed into a square disc, and silver paste was used as the contact electrode. Nitrogen adsorption-desorption isotherms and pore size distribution were recorded on ASAP 2020 M (Micromeritics) under liquid nitrogen temperature. The contact angle was measured by a Solon SL200B automatic contact angle meter.

Electrochemical measurements. The sodium storage performance of the materials was evaluated by assembling CR2032 coin-type cells. The working electrode slurry was prepared by mixing the active material, conductive carbon black (Super P), and sodium alginate (SA) in a mass ratio of 8:1:1 with deionized water as the solvent. Then the slurry was uniformly coated on copper foil and dried under vacuum at 90 °C for 12 h. After that, the foil was punched into 12 mm discs. The mass loading of the active material on each disc is ~1.2 mg cm^{-2}. The half cells were assembled with fresh sodium foil as the counter electrode and glass fiber (GF/D, Whatman) as the separator in an argon-filled glove box (MBRAUN-LABstar, with H_2O and O_2 levels < 0.5 ppm). The

electrolyte was 1.0 M sodium hexafluorophosphate ($NaPF_6$) dissolved in diethylene glycol dimethyl ether (DEGDME). To prepare $Mo_2S_3||Na_3V_2(PO_4)_3$ full cell, the freestanding Mo_2S_3 anode was prepared by mixing Mo_2S_3, Super P, and polytetrafluoroethylene (PTFE) in a mass ratio of 8:1:1 with isopropanol as the solvent. Then the slurry was ground until the solvent evaporates and rolled into a thin film to obtain the freestanding Mo_2S_3 anode. The as-prepared anode was pre-sodiated in a half cell for 3 cycles before assembling the full cell. The $Na_3V_2(PO_4)_3$ (NVP) cathode was obtained from Shenzhen Kejing Star Technology Co., Ltd. The cathode slurry was prepared by mixing NVP, Super P, and polyvinylidene difluoride (PVDF) in a mass ratio of 8:1:1 with N-methyl-2-pyrrolidone (NMP) as the solvent, and the slurry was uniformly coated on an aluminum foil and dried under vacuum at 100 °C for 12 h. The mass ratio of the cathode to the anode was controlled at ~4.5: 1 to balance the capacity. The specific capacity of the full cell was calculated based on the mass of the cathode. The separator and electrolyte were consistent with those in half cells. The charge-discharge and galvanostatic intermittent titration technique (GITT) tests were carried out on LAND-CT2001A test system at different current densities. The GITT was performed through a pulse current of 100 mA g^{-1} for 10 min followed by relaxation intervals of 40 min. Cyclic voltammogram (CV) from 0.01 to 3.0 V and electrochemical impedance spectroscopy (EIS) over the frequency from 100 kHz to 0.1 Hz were measured by CHI760E electrochemical workstation (Chenhua, Shanghai).

Theoretical capacity calculations. The electrode reactions of Mo_2S_3 anode based on

our results are summarized as follows:

$Mo_2S_3 + 6\ Na^+ + 6\ e^- \rightarrow 2\ Mo + 3\ Na_2S$

The theoretical capacity (1 C = 558 mA g^{-1}) is calculated according to the following formula:

$$C_t = \frac{nF}{3.6M_r}$$

Where n is the number of transferred electrons, F is the Faraday constant (96485 C mol^{-1}), and M_r is the molar mass of Mo_2S_3 (288 g mol^{-1}).

Carrier concentration calculations. The carrier concentration n is calculated according to the following formula:

$$slope = \frac{R_{hall}}{B} = \frac{W_e}{DqW_s}\frac{1}{n}$$

Where R_{hall} is the Hall resistance of the sample, B is the magnetic flux density, W_e is the distance between electrodes, W_s is the width of the sample, D is the height of the sample along the direction of B, and q is the charge of the carrier (1.6×10^{-19} C).

Density functional theory calculations. Density functional theory (DFT) calculations were performed with the Vienna *ab initio* simulation package (VASP), using the plane-wave basis with an energy cutoff of 500 eV,[S1] projector augmented wave (PAW) potentials,[S2] and the generalized gradient approximation (GGA)[S3] with the Perdew−Burke−Ernzerhof (PBE) exchange-correlation functional. All structures were relaxed by a conjugate gradient (CG) method until the residual force component was less than 0.02 eV/Å, and the convergence criterion of total energy in the self-consistent

field method was set to 10^{-8} eV. For analyses of the band structure and the density of states, further calculations were performed using Heyd–Scuseria–Ernzerhof hybrid functional (HSE06),[S4] and the corresponding residual force component was less than 0.01 eV/Å, while a convergence criterion of 10^{-6} eV was employed. As for the adsorption and migration calculations, the vacuum space was set to be 15 Å to separate the interactions between the neighboring slabs. In this calculation, a 1×1×1 k-point mesh was adopted for both Mo_2S_3 (001) and MoS_2 (001). The climbing image-nudged elastic band (CINEB) method[S5] was also employed for sodium ion migration calculations.

Supplementary Note. **Small polaron.**

In condensed matter physics, a polaron is a quasiparticle that can be used to study the interactions between electrons and atoms in a solid material. The polaron concept was proposed by Lev Landau[S6] and Solomon Pekar[S7] to describe an electron moving in a dielectric crystal where the atoms displace from their equilibrium positions to effectively screen the charge of an electron, known as a phonon cloud. The existence of the small polarons will lower the electron mobility and increases the electron's effective mass (localization).

According to previous studies in Li-ion battery[S8-10] and perovskite structures[S11-13], polaron preemption/polaron collapse is generally employed to accelerate carrier transport. In addition, the existence of small polarons in bulk MoS_2 has also been reported in previous work,[S14, S15] and it would be destroyed in the monolayer MoS_2.[S15]

Supplementary Figures

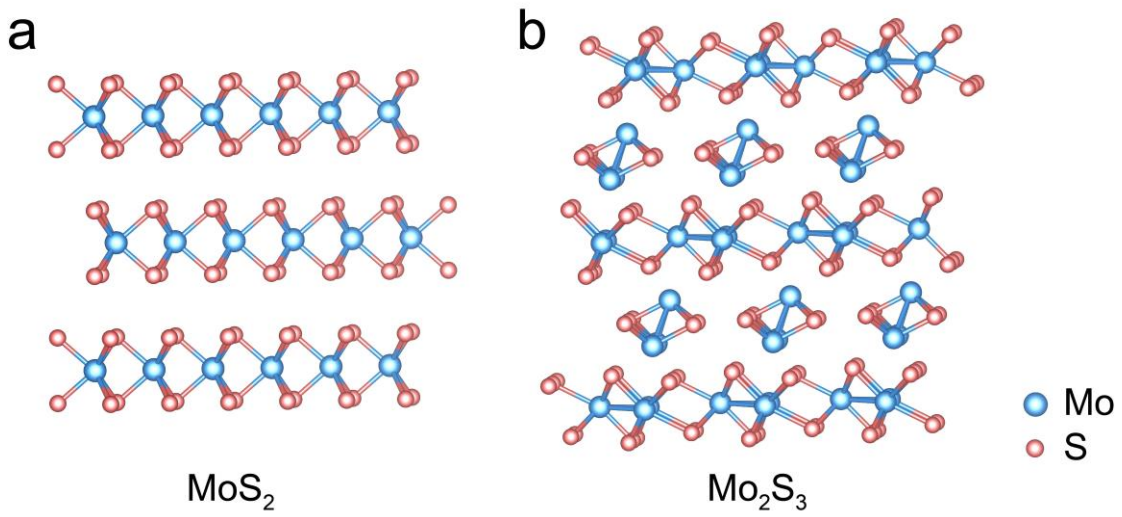

Supplementary Figure 1. The optimized crystal structure of a) MoS_2 and b) Mo_2S_3.

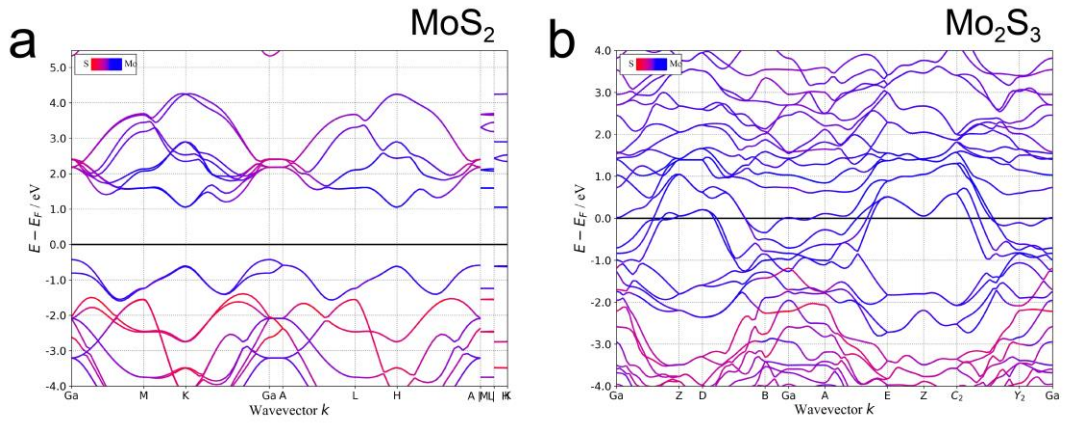

Supplementary Figure 2. The band structure of a) MoS_2 and b) Mo_2S_3. Ga = Gamma point.

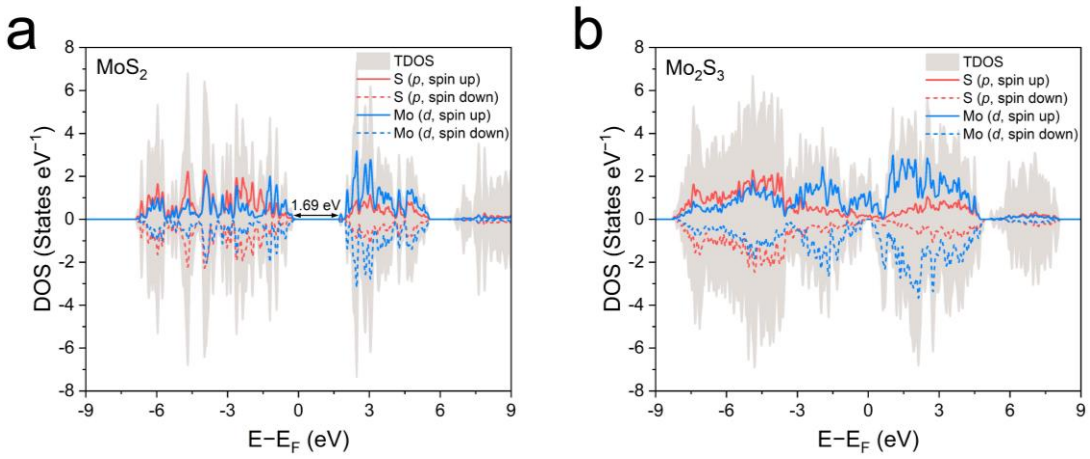

Supplementary Figure 3. The density of states (DOS) for a) Mo_2S_3 and b) MoS_2.

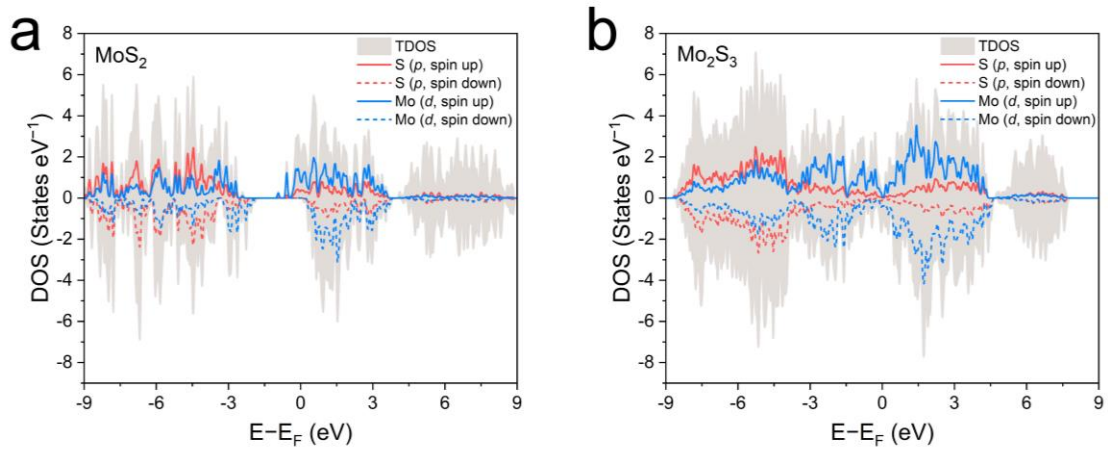

Supplementary Figure 4. The density of states (DOS) with an excess electron injection for a) MoS_2 and b) Mo_2S_3.

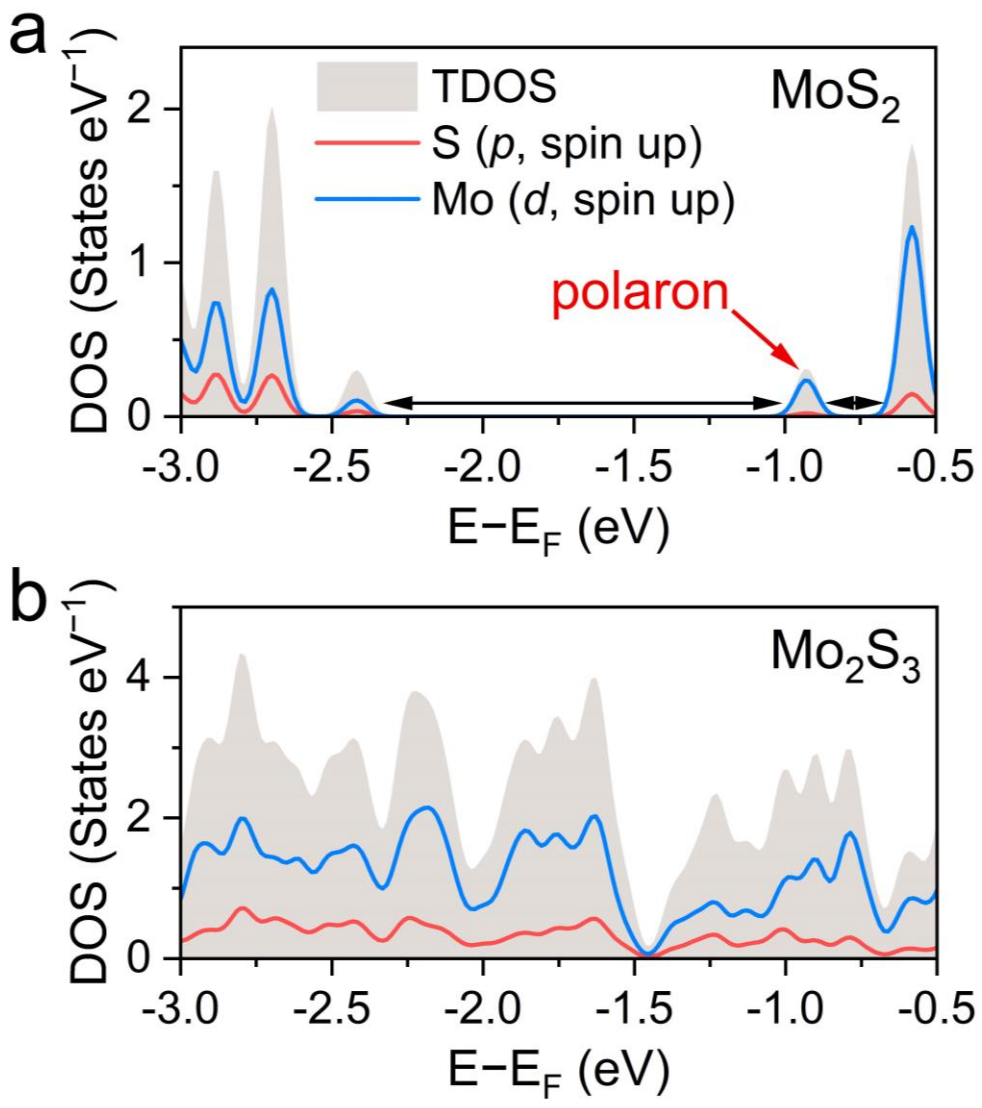

Supplementary Figure 5. Enlarged DOS patterns for a) MoS_2 with an injected electron and b) Mo_2S_3 with an injected electron.

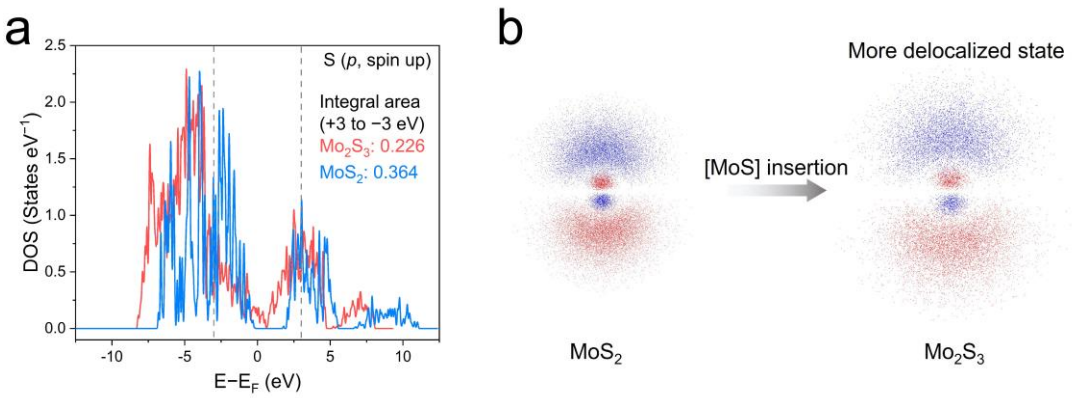

Supplementary Figure 6. a) DOS of S *p*-orbitals (spin up) in MoS_2 and Mo_2S_3. b) Schematic illustration of the delocalized *p*-electron cloud of S^{2-} in Mo_2S_3 induced by [MoS] insertion.

Exhibition of the ratio of DOS near the Fermi level (e.g., +3 to −3 eV) can describe the feature of electron states.[S16, S17] We have calculated the integral area ratio of DOS ranging from +3 to −3 eV, and the value of Mo_2S_3 is calculated to be 0.226, which is much smaller than that of MoS_2 (0.364). The smaller integral area ratio in Mo_2S_3 demonstrates a delocalized electron state with enhanced electron cloud dispersion around each S^{2-}.

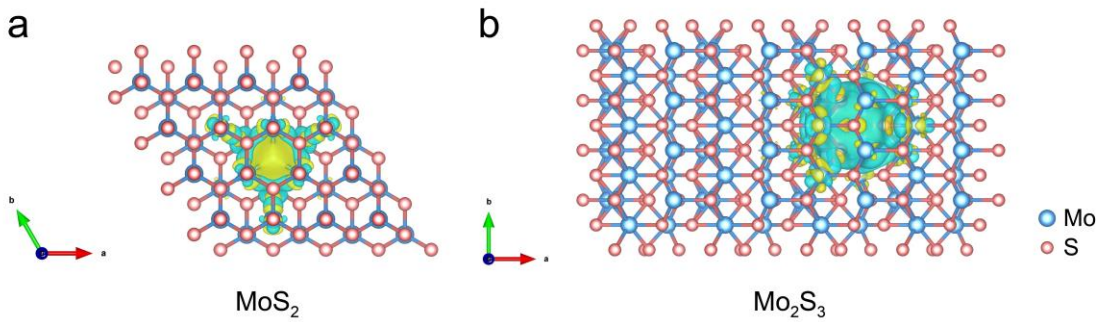

Supplementary Figure 7. Charge difference plots for a) MoS_2 (001) slab with Na atom and b) Mo_2S_3 (001) slab with Na atom.

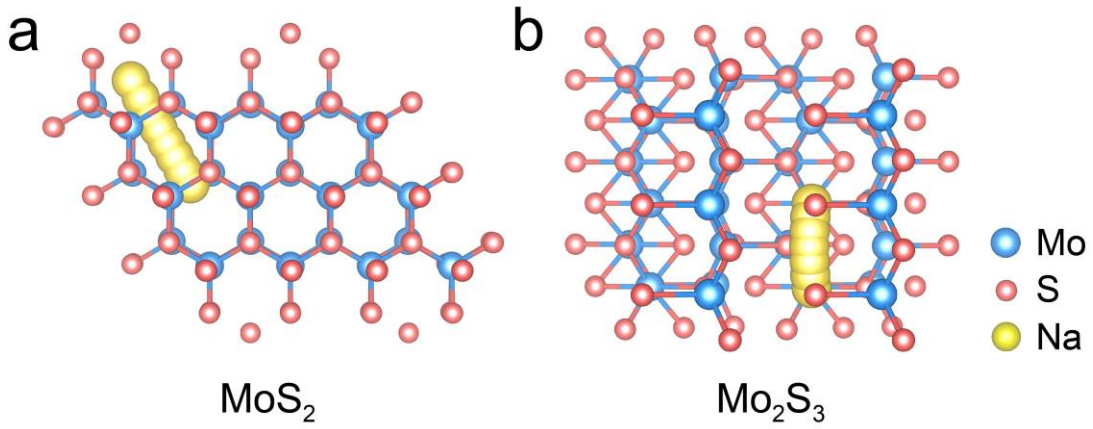

Supplementary Figure 8. Migration paths for Na^+ diffusion in a) MoS_2 (001) slab and b) Mo_2S_3 (001) slab.

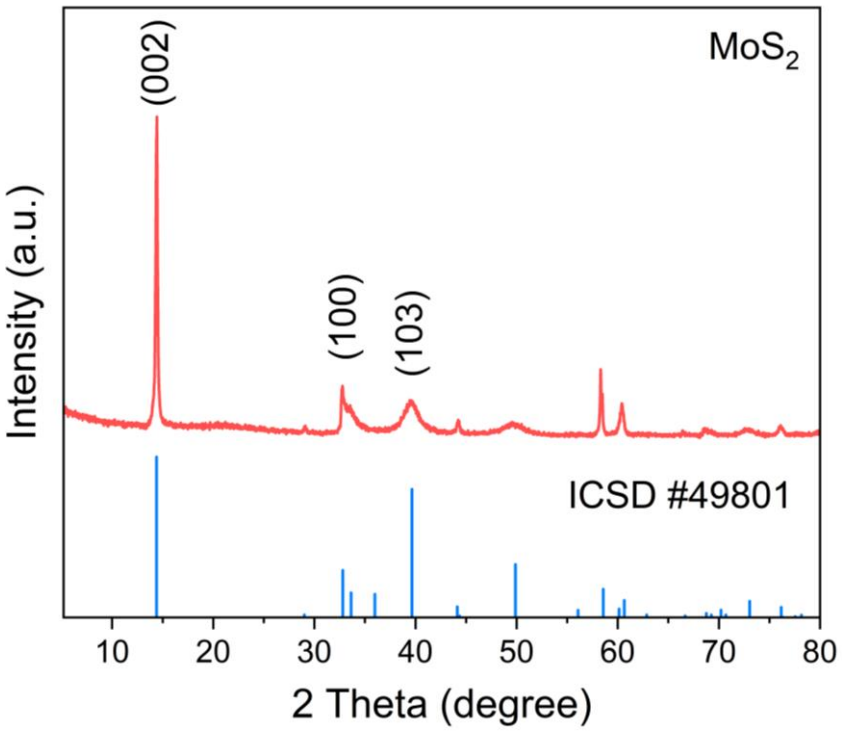

Supplementary Figure 9. XRD pattern of MoS_2.

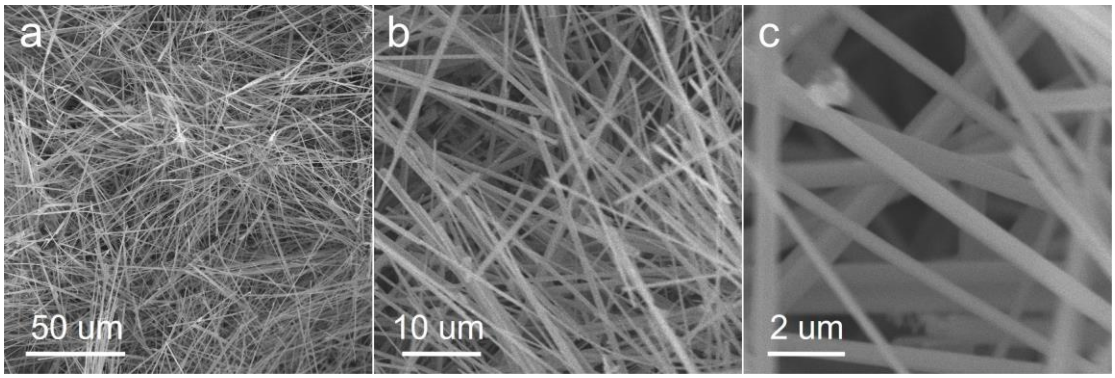

Supplementary Figure 10. a-c) SEM images of Mo_2S_3.

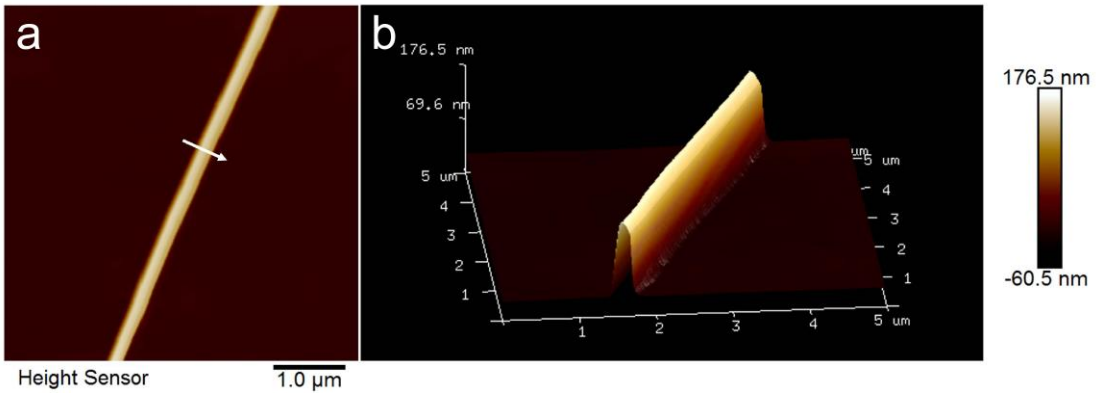

Supplementary Figure 11. a) AFM image and b) 3D height profiles along the white arrow of Mo_2S_3.

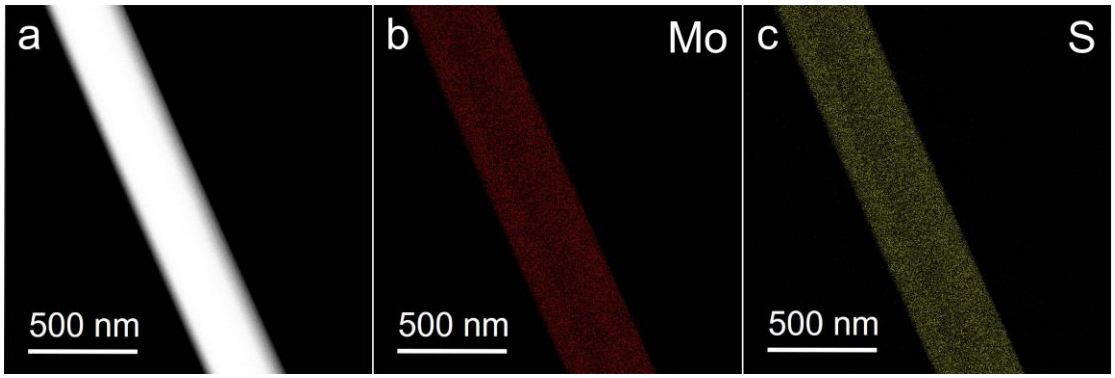

Supplementary Figure 12. a) HAADF-STEM image of Mo_2S_3. EDS mapping of b) Mo and c) S.

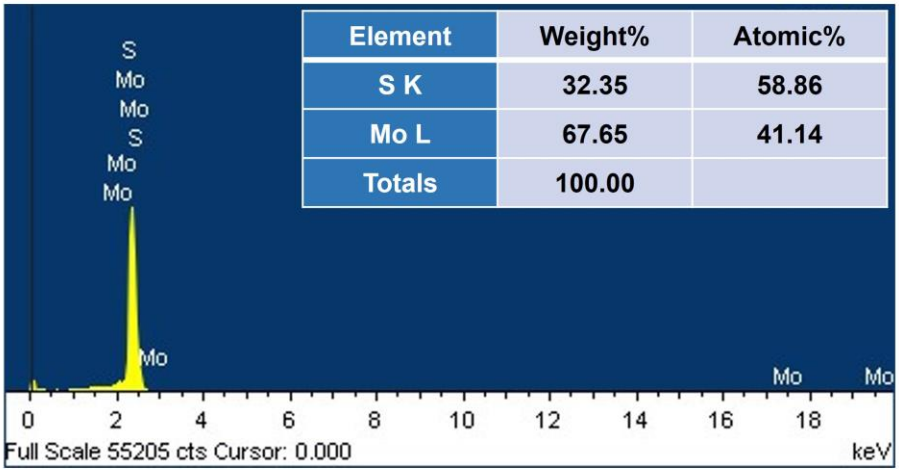

Element	Weight%	Atomic%
S K	32.35	58.86
Mo L	67.65	41.14
Totals	100.00	

Supplementary Figure 13. EDS results of Mo_2S_3.

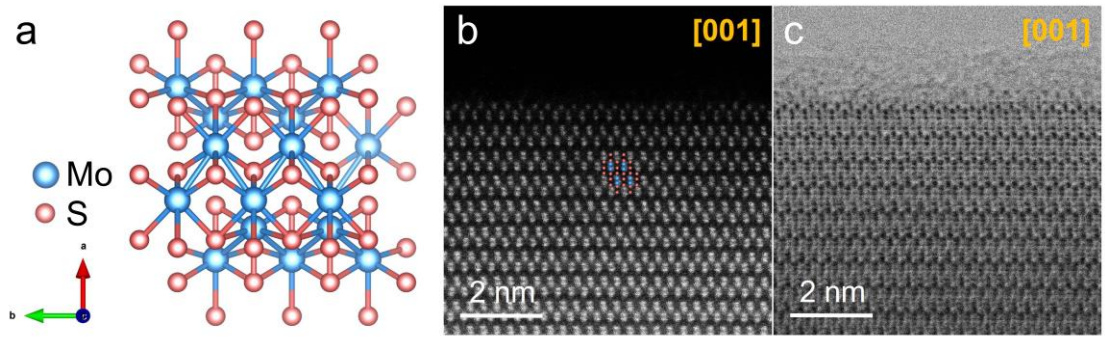

Supplementary Figure 14. a) Crystal structure of Mo_2S_3 in the *c*-direction. b) ADF-STEM image and c) ABF-STEM image of Mo_2S_3.

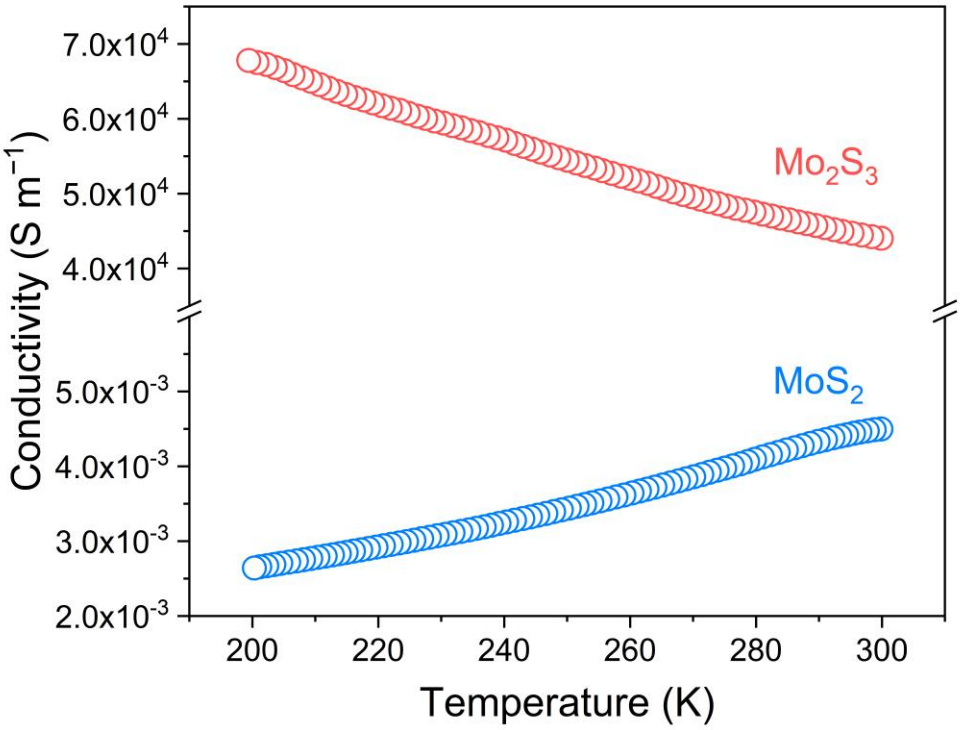

Supplementary Figure 15. Temperature-dependent electrical conductivity curves of Mo_2S_3 and MoS_2.

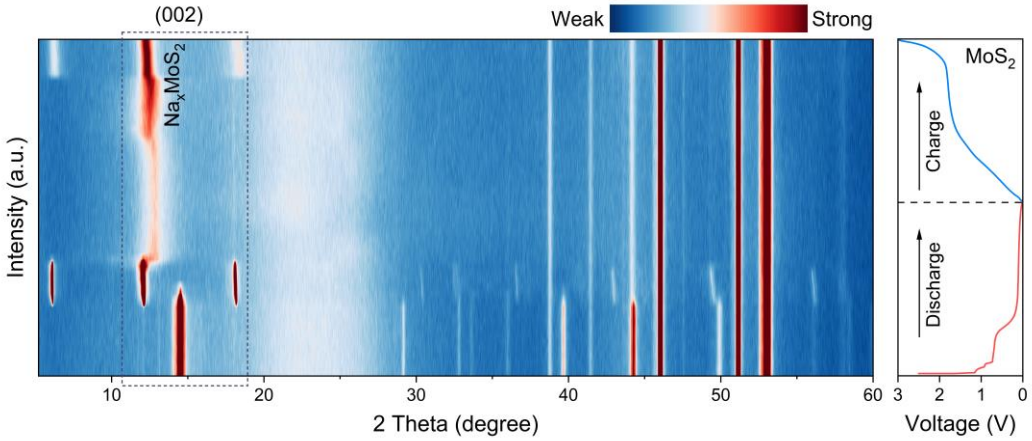

Supplementary Figure 16. In situ XRD patterns of MoS_2 in the first cycle.

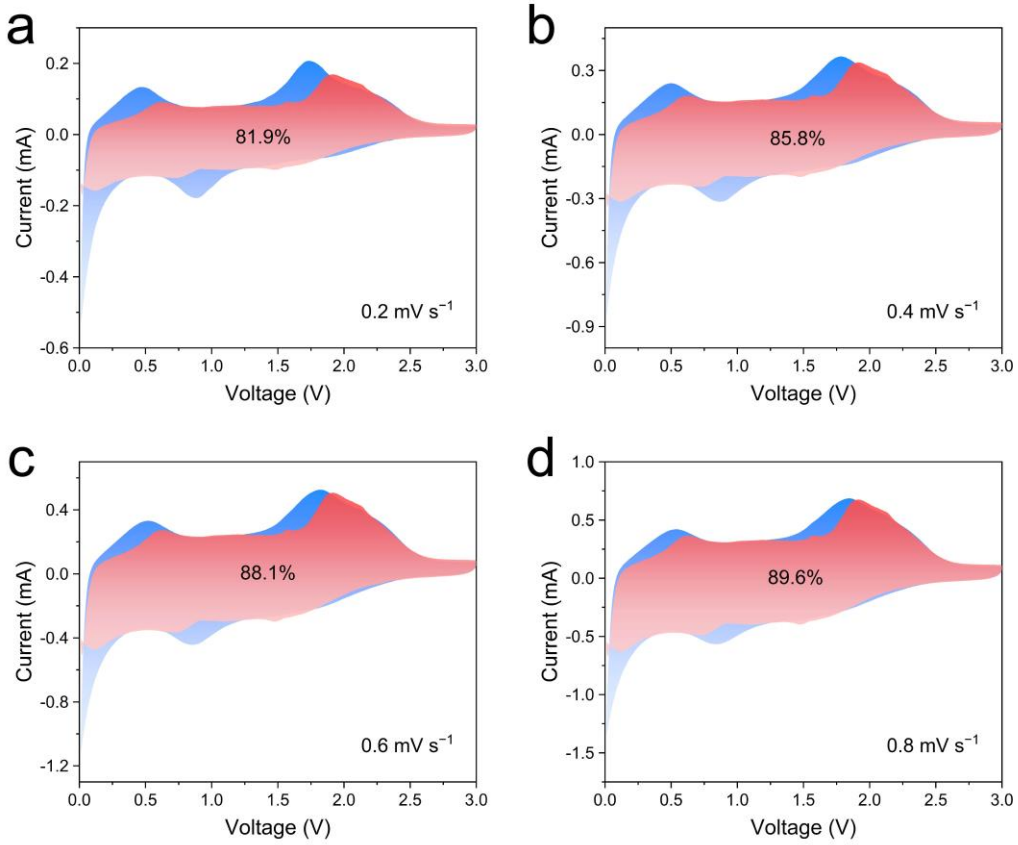

Supplementary Figure 17. CV curves of Mo_2S_3 with a pseudocapacitive contribution at a) 0.2 mV s^{-1}, b) 0.4 mV s^{-1}, c) 0.6 mV s^{-1}, and d) 0.8 mV s^{-1}.

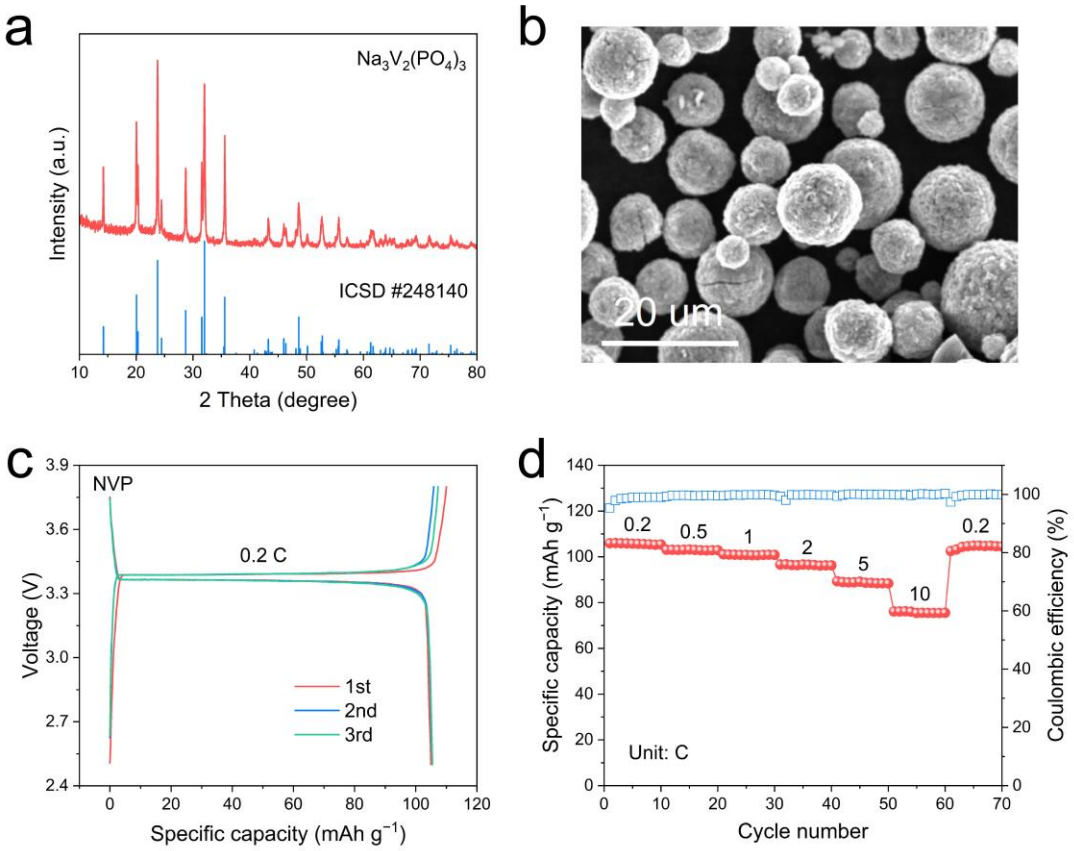

Supplementary Figure 18. a) XRD pattern and b) SEM image of NVP. c) GCD curves for the initial three cycles and d) Rate capability of NVP in half cells (1 C = 117.6 mA g^{-1}).

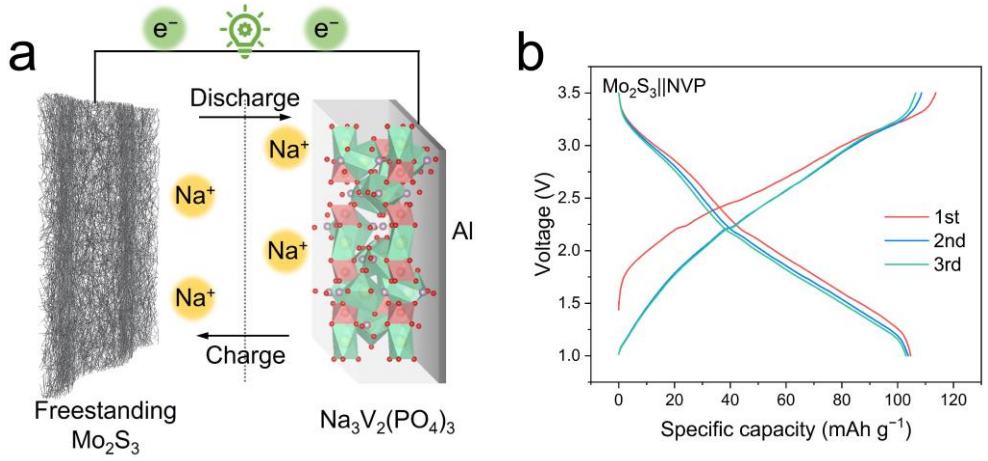

Supplementary Figure 19. a) Schematic diagram of assembled Mo_2S_3||NVP full cell. b) GCD curves of the Mo_2S_3||NVP full cell in the initial three cycles at 0.2 C.

References

S1. Kresse G, Furthmuller J. Efficient iterative schemes for ab initio total-energy calculations using a plane-wave basis set. *Physical Review B* **54,** 11169-11186 (1996).

S2. Kresse G, Joubert D. From ultrasoft pseudopotentials to the projector augmented-wave method. *Physical Review B* **59,** 1758 (1999).

S3. Perdew JP, Burke K, Ernzerhof M. Generalized gradient approximation made simple. *Physical Review Letters* **77,** 3865-3868 (1996).

S4. Heyd J, Scuseria GE, Ernzerhof M. Hybrid functionals based on a screened Coulomb potential. *The Journal of Chemical Physics* **118,** 8207-8215 (2003).

S5. Henkelman G, Uberuaga BP, Jonsson H. A climbing image nudged elastic band method for finding saddle points and minimum energy paths. *Journal of Chemical Physics* **113,** 9901-9904 (2000).

S6. Landau LD. Electron motion in crystal lattices. *Phys. Z. Sowjetunion* **3,** 664 (1933).

S7. Pekar SI. Local quantum states of electrons in an ideal ion crystal. *J. Phys. USSR* **10,** 341 (1946).

S8. Ellis B, Perry LK, Ryan DH, Nazar LF. Small polaron hopping in Li_xFePO_4 solid solutions: coupled lithium-ion and electron mobility. *Journal of the American Chemical Society* **128,** 11416-11422 (2006).

S9. Kang J, Jung YS, Wei S-H, Dillon AC. Implications of the formation of small polarons in Li_2O_2 for Li-air batteries. *Physical Review B* **85,** 035210 (2012).

S10. Goodenough JB, Park K-S. The Li-ion rechargeable battery: A perspective. *Journal of the American Chemical Society* **135,** 1167-1176 (2013).

S11. Neukirch AJ, Nie W, Blancon J-C, Appavoo K, Tsai H, Sfeir MY*, et al.* Polaron stabilization by cooperative lattice distortion and cation rotations in hybrid perovskite materials. *Nano Letters* **16,** 3809-3816 (2016).

S12. Kahmann S, Tekelenburg EK, Duim H, Kamminga ME, Loi MA. Extrinsic nature of the broad photoluminescence in lead iodide-based Ruddlesden–Popper perovskites. *Nature Communications* **11,** 2344 (2020).

S13. Tao W, Zhang Y, Zhu H. Dynamic exciton polaron in two-dimensional lead halide perovskites and implications for optoelectronic applications. *Accounts of Chemical Research* **55,** 345-353 (2022).

S14. Kang M, Jung SW, Shin WJ, Sohn Y, Ryu SH, Kim TK*, et al.* Holstein polaron in a valley-degenerate two-dimensional semiconductor. *Nature Materials* **17,** 676-680 (2018).

S15. Roch JG, Froehlicher G, Leisgang N, Makk P, Watanabe K, Taniguchi T*, et al.* Spin-polarized electrons in monolayer MoS_2. *Nat Nanotechnol* **14,** 432-436 (2019).

S16. Kong S, Lv X, Wang X, Liu Z, Li Z, Jia B*, et al.* Delocalization state-induced selective bond breaking for efficient methanol electrosynthesis from CO_2. *Nature Catalysis* **6,** 6-15 (2023).

S17. Lv Z, Peng B, Lv X, Gao Y, Hu K, Dong W*, et al.* Intercalative motifs-induced space confinement and bonding covalency enhancement enable ultrafast and large sodium storage. *Advanced Functional Materials* 2214370 (2023).